^{78}Ni revealed as a doubly magic stronghold against nuclear deformation

R. Taniuchi,[1,2] C. Santamaria,[3,2] P. Doornenbal,[2,*] A. Obertelli,[3,2,4] K. Yoneda,[2] G. Authelet,[3] H. Baba,[2] D. Calvet,[3] F. Château,[3] A. Corsi,[3] A. Delbart,[3] J.-M. Gheller,[3] A. Gillibert,[3] J.D. Holt,[5] T. Isobe,[2] V. Lapoux,[3] M. Matsushita,[6] J. Menéndez,[6] S. Momiyama,[1,2] T. Motobayashi,[2] M. Niikura,[1] F. Nowacki,[7] K. Ogata,[8,9] H. Otsu,[2] T. Otsuka,[6,1,2] C. Péron,[3] S. Péru,[10] A. Peyaud,[3] E.C. Pollacco,[3] A. Poves,[11] J.-Y. Roussé,[3] H. Sakurai,[1,2] A. Schwenk,[4,12,13] Y. Shiga,[2,14] J. Simonis,[15,4,12] S.R. Stroberg,[5,16] S. Takeuchi,[2] Y. Tsunoda,[6] T. Uesaka,[2] H. Wang,[2] F. Browne,[17] L.X. Chung,[18] Zs. Dombradi,[19] S. Franchoo,[20] F. Giacoppo,[21] A. Gottardo,[20] K. Hadyńska-Klęk,[21] Z. Korkulu,[19] S. Koyama,[1,2] Y. Kubota,[2,6] J. Lee,[22] M. Lettmann,[4] C. Louchart,[4] R. Lozeva,[7,23] K. Matsui,[1,2] T. Miyazaki,[1,2] S. Nishimura,[2] L. Olivier,[20] S. Ota,[6] Z. Patel,[24] E. Şahin,[21] C. Shand,[24] P.-A. Söderström,[2] I. Stefan,[20] D. Steppenbeck,[6] T. Sumikama,[25] D. Suzuki,[20] Zs. Vajta,[19] V. Werner,[4] J. Wu,[2,26] and Z.Y. Xu[22]

[1]*Department of Physics, The University of Tokyo, 7-3-1 Hongo, Bunkyo, Tokyo 113-0033, Japan*
[2]*RIKEN Nishina Center, 2-1 Hirosawa, Wako, Saitama 351-0198, Japan*
[3]*IRFU, CEA, Université Paris-Saclay, F-91191 Gif-sur-Yvette, France*
[4]*Institut für Kernphysik, Technische Universität Darmstadt, 64289 Darmstadt, Germany*
[5]*TRIUMF 4004 Wesbrook Mall, Vancouver, British Columbia, Canada V6T 2A3*
[6]*Center for Nuclear Study, The University of Tokyo, RIKEN campus, Wako, Saitama 351-0198, Japan*
[7]*IPHC, CNRS/IN2P3, Université de Strasbourg, F-67037 Strasbourg, France*
[8]*Research Center for Nuclear Physics, Osaka University, Ibaraki 567-0047, Japan*
[9]*Department of Physics, Osaka City University, Osaka 558-8585, Japan*
[10]*CEA, DAM, DIF, 91297 Arpajon, France*
[11]*Departamento de Física Teorica and IFT-UAM/CSIC, Universidad Autónoma de Madrid, 28049 Madrid, Spain*
[12]*ExtreMe Matter Institute EMMI, GSI Helmholtzzentrum für Schwerionenforschung GmbH, 64291 Darmstadt, Germany*
[13]*Max-Planck-Institut für Kernphysik, Saupfercheckweg 1, 69117 Heidelberg, Germany*
[14]*Department of Physics, Rikkyo University, 3-34-1 Nishi-Ikebukuro, Toshima, Tokyo 172-8501, Japan*
[15]*Institut für Kernphysik and PRISMA Cluster of Excellence, Johannes Gutenberg-Universität Mainz, 55128 Mainz, Germany*
[16]*Physics Department, Reed College, 3203 SE Woodstock Blvd., Portland, OR 97202-8199, USA*
[17]*School of Computing, Engineering and Mathematics, University of Brighton, Brighton BN2 4GJ, United Kingdom*
[18]*Institute for Nuclear Science & Technology, VINATOM, P.O. Box 5T-160, Nghia Do, Hanoi, Vietnam*
[19]*MTA Atomki, P.O. Box 51, Debrecen H-4001, Hungary*
[20]*Institut de Physique Nucléaire, CNRS/IN2P3, Université Paris-Saclay, F-91406 Orsay Cedex, France*
[21]*Department of Physics, University of Oslo, N-0316 Oslo, Norway*
[22]*Department of Physics, The University of Hong Kong, Pokfulam, Hong Kong*
[23]*CSNSM, CNRS/IN2P3, Université Paris-Saclay, F-91405 Orsay Campus, France*
[24]*Department of Physics, University of Surrey, Guildford GU2 7XH, United Kingdom*
[25]*Department of Physics, Tohoku University, Sendai 980-8578, Japan*
[26]*State Key Laboratory of Nuclear Physics and Technology, Peking University, Beijing 100871, P.R. China*

(Dated: February 10, 2019)

Nuclear magic numbers, which emerge from the strong nuclear force based on quantum chromodynamics, correspond to fully occupied energy shells of protons, or neutrons inside atomic nuclei. Doubly magic nuclei, with magic numbers for both protons and neutrons, are spherical and extremely rare across the nuclear landscape. While the sequence of magic numbers is well established for stable nuclei, evidence reveals modifications for nuclei with a large proton-to-neutron asymmetry. Here, we provide the first spectroscopic study of the doubly magic nucleus ^{78}Ni, fourteen neutrons beyond the last stable nickel isotope. We provide direct evidence for its doubly magic nature, which is also predicted by *ab initio* calculations based on chiral effective field theory interactions and the quasi-particle random-phase approximation. However, our results also provide the first indication of the breakdown of the neutron magic number 50 and proton magic number 28 beyond this stronghold, caused by a competing deformed structure. State-of-the-art phenomenological shell-model calculations reproduce this shape coexistence, predicting further a rapid transition from spherical to deformed ground states with ^{78}Ni as turning point.

Characterisation of the few doubly magic nuclei, known and predicted, provides a benchmark for our knowledge of the fundamental forces that drive the evolution of shell closures with proton-to-neutron asymme-

* pieter@ribf.riken.jp

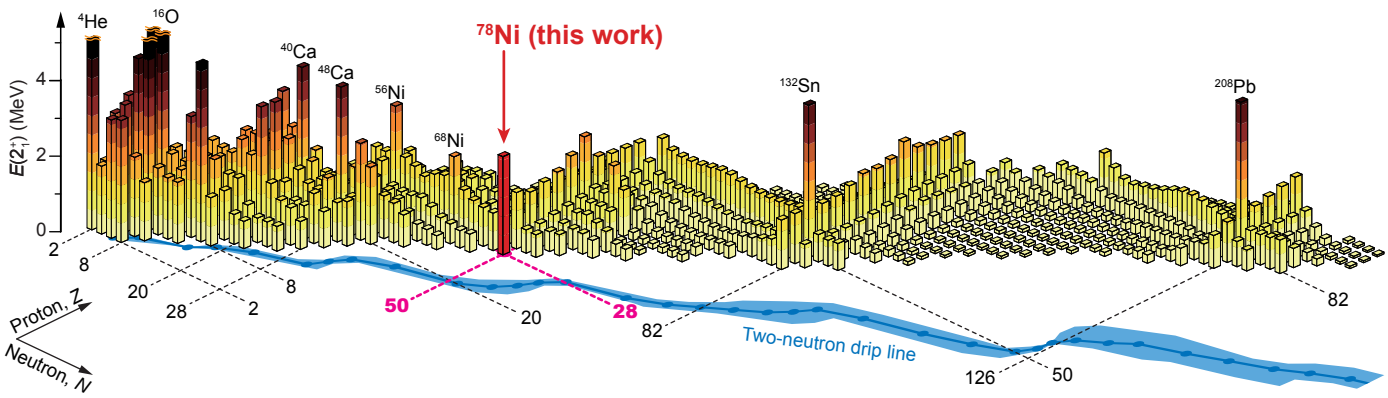

Fig. 1 | Experimental $E(2_1^+)$ systematics of the even-even nuclear landscape. Shown are known $E(2_1^+)$ of even-even isotopes[40] and the value for ^{78}Ni obtained in the present study. Traditional magic numbers are indicated by dashed lines and doubly magic nuclei are labelled. Also ^{68}Ni, for which the number of neutrons, $N = 40$, matches the harmonic oscillator shell closure, is marked. The predicted two-neutron drip line and its uncertainties[3] are shown in blue.

try[1,2]. With reliable and globally applicable interactions, accurate predictions of the location of the two-neutron drip line and the nuclear landscape can be made[3]. These, in turn, are critical for nucleosynthesis models, which rely on nuclear structure inputs.

An initial characterisation of magicity is often provided by the first $J^\pi = 2^+$ excitation energy, $E(2_1^+)$, as illustrated in Fig. 1 for the Segrè chart, a two-dimensional grid in which nuclei are arranged by their proton (Z) and neutron (N) numbers. Magic nucleon numbers (2, 8, 20, 28, 50, 82, 126), which were first correctly reproduced theoretically for stable isotopes by introducing a strong spin-orbit interaction[4,5], stand out, as excitation from the ground state requires promoting nucleons across major nuclear shells, and, therefore, more energy due to the large energy gaps involved. Further experimental observables, such as charge radii or reduced γ-ray transition probabilities, are indispensable for a comprehensive characterisation of a nucleus. Their acquisition is, however, experimentally challenging.

With the extension of studies to unstable, radioactive isotopes (RIs) with a large neutron excess – also termed 'exotic' nuclei –, magic numbers emerged as a local feature. In lieu, nuclear shell structure changes, sometimes drastically, with the number of protons and neutrons, revealing interesting properties of the underlying nuclear forces. For instance, it was recognised that several traditional neutron magic numbers disappear far from stability, such as $N = 8, 20, 28$[6–9], while new ones have been claimed at $N = 16$[10] and $N = 32, 34$[1,2,11].

Shifts of these magic numbers challenge nuclear theory, and certain cases can be explained by drifts of the single-particle orbitals (SPOs) with varying nucleon number[12]. The central potential of the nucleon-nucleon (NN) effective interaction and the tensor force contribute strongly to this evolution[13,14]. Also three-nucleon ($3N$) forces, which originate from the composite nature of nucleons, have a significant impact[15,16]. So far, a coherent picture of the nuclear shell structure and its evolution towards the most neutron-rich nuclei remains elusive.

The isotope ^{78}Ni (28 protons and 50 neutrons) provides a unique case included in all motivations for planned and operating next-generation RI beam in-flight facilities, such as the RIBF in Japan, FRIB in the USA, and FAIR in Germany. Predictions regarding the neutron drip-line location[3] of even-even nuclei, for which the two-neutron separation energy becomes negative (also shown in Fig. 1), reveal that, prior to the measurement reported here, ^{78}Ni was the only neutron-rich doubly magic nucleus lacking spectroscopic information on excited states that can be reached with current and next-generation facilities.

After the first production of ^{78}Ni[17], enormous efforts have been put into investigating its structure. Previous measurements indirectly inferred persistent $N = 50$[18–22] and $Z = 28$[23–25] shell closures at ^{78}Ni. This notion has been reinforced theoretically by *ab initio* predictions[27]. Conversely, studies of ^{66}Cr ($Z = 24$) and ^{70,72}Fe ($Z = 26$) revealed constantly low excitation energies that question the $N = 50$ shell closure for proton numbers below $Z = 28$[26,28]. Likewise, several studies supported a reduction of the $Z = 28$ proton shell gap towards and beyond $N = 50$[29–33]. A vanishing of the proton and neutron shell closures would be accompanied by an onset of deformation, implying dramatic consequences: Shape coexistence and gain in nuclear binding energy. The former signifies occurrence of several quantum states of different shapes lying close and low in energy, the latter slants the two-neutron drip line and accordingly the limits of nuclear existence towards heavier isotopes. Hitherto, no ul-

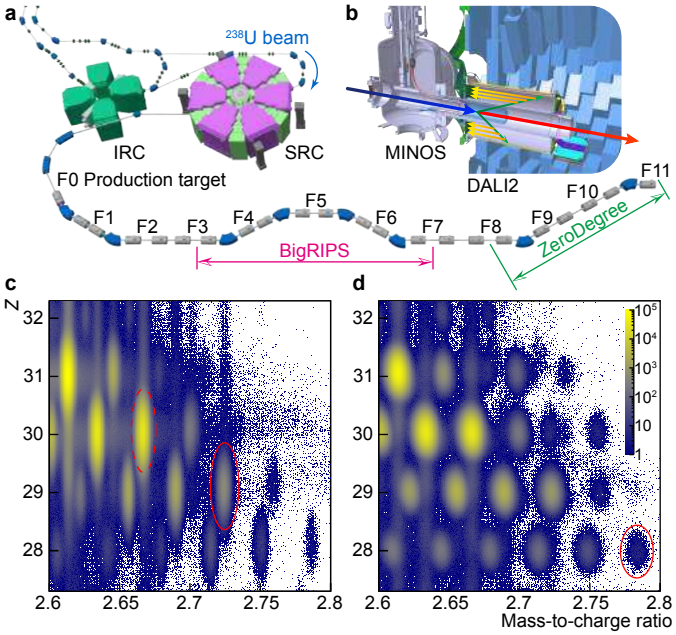

Fig. 2 | Layout of the experimental equipment and particle identification plots of isotopes. **a**, Schematic view of the final two cyclotron stages, IRC and SRC, of the RIBF facility along with the BigRIPS and ZeroDegree fragment separators. Reaction residues cover a flight length of 118 m between creation at the F0 production target and the final focal point, F11. **b**, A layout of MINOS and the surrounding DALI2 γ-ray spectrometer located at the F8 focal plane. **c**, Components of the radioactive beam accepted by the BigRIPS fragment separator. Events corresponding to ^{79}Cu (red ellipse) and ^{80}Zn (dashed red ellipse) are indicated. **d**, Reaction products accepted by ZeroDegree. ^{78}Ni is enclosed by the red ellipse. Both plots in **c**, **d** share the colour scale that indicates the number of events for the different isotopes transmitted through BigRIPS and ZeroDegree.

timate conclusion on the magic character of ^{78}Ni existed. Here, we provide first direct evidence from in-beam γ-ray spectroscopy in prompt coincidence with proton removal reactions of fast RI beams.

Production of RI beams

The experiment was carried out at the RIBF, which combines three injectors with four coupled cyclotrons. Neutron-rich RI beams were produced by induced relativistic in-flight fission of a 345 MeV/u ^{238}U primary beam on a 3-mm-thick beryllium production target, located at the F0 focus of the BigRIPS fragment separator[34] shown in Fig. 2a. ^{79}Cu and ^{80}Zn particles, produced at rates of 5 and 290 particles per second, respec-

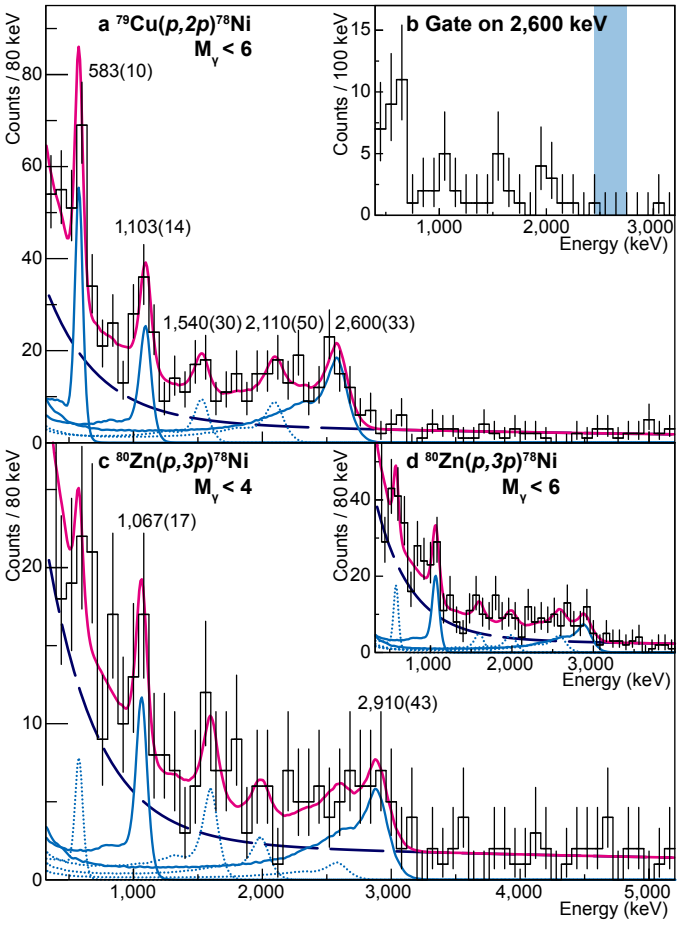

Fig. 3 | Doppler-corrected γ-ray energy spectra. **a**, De-excitation γ rays measured in coincidence with ^{78}Ni following $(p, 2p)$ reactions. **b**, Prompt coincidences with the 2,600-keV transition following $(p, 2p)$ reactions. It reveals coincidences between the 2,600-keV and other low-lying transitions. The coincidence range is illustrated by the hatched area. **c**, De-excitation γ rays measured in coincidence with ^{78}Ni following $(p, 3p)$ reactions. To reduce events with multiple γ-ray hits from Compton scattering, the γ-ray detection multiplicity, M_γ, was restricted to values below four. As a consequence, the visibility of the 2,910-keV transition is enhanced. **d**, Same as **c**, but for the $M_\gamma < 6$ condition. Observed transitions are indicated by their energies in **a** and **c**. Simulated response curves of the γ-ray detector for the individual transitions are illustrated by the light-blue solid (S.L. ≥ 3) and dotted (S.L. < 3) lines, while the fitted double-exponential background is shown by the dark-blue dashed line. Background and individual transitions are summed for the magenta solid lines. Vertical error bars correspond to 1 s.d. errors.

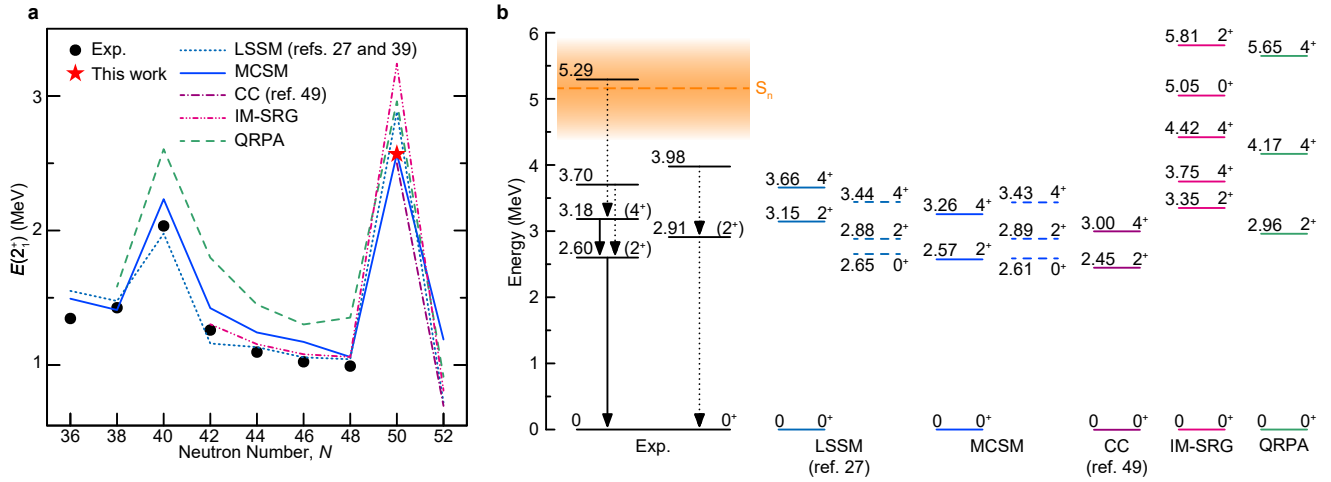

Fig. 4 | Comparison of theoretical predictions with experimental data. **a**, Experimental $E(2_1^+)$ for even-even nickel isotopes are compared to calculations using phenomenological shell-model interactions, LSSM[28,41] (dotted line) and MCSM[43] (solid line), the beyond mean field approach, QRPA (dashed line), and the *ab initio* approach, IM-SRG (dash-dot-dotted line) and CC[27] (dash-dotted line), as a function of their neutron number, N. The present result for ^{78}Ni is indicated by the red star. **b**, Deduced experimental level scheme compared to detailed theoretical calculations for ^{78}Ni. Transitions with S.L. ≥ 5 are represented by solid arrows. Dotted arrows correspond to values S.L. < 5. The 1.54-MeV transition is not placed, while the 2.11-MeV transition has a S.L. < 3. The evaluated neutron separation energy, S_n, and its errors[50] are indicated by the orange dashed line and area, respectively. Predicted deformed states are indicated by dashed lines. For convenience, theoretical predictions show only the two lowest 0^+, 2^+, and 4^+ spin-parity values.

tively, were identified on an event-by-event basis from focal plane F3 to F7, before being guided to the MINOS reaction target system[35] (see Fig. 2b) located at F8 with a remaining energy of approximately 250 MeV/u (61% of the speed of light).

γ-ray detection after secondary reaction

MINOS was composed of a 102(1)-mm-thick liquid hydrogen target and a time projection chamber to reconstruct the reaction vertices. This allowed to overcome inaccuracies in the Doppler reconstruction originating from the thick target (see Methods for details). DALI2[36] surrounded MINOS to detect prompt de-excitation γ rays with high efficiency. Secondary reaction species were subsequently identified with the ZeroDegree spectrometer from F8 to F11. An overview of the facility and the experimental set-up, including all the focal points, is provided in Fig. 2 together with obtained particle identification plots.

γ rays from the ^{79}Cu$(p,2p)^{78}$Ni reaction

Inclusive reaction cross sections for the production of ^{78}Ni following the ^{79}Cu$(p,2p)^{78}$Ni and ^{80}Zn$(p,3p)^{78}$Ni reactions were 1.70(42) and 0.016(6) mbarn, respectively, yielding 937 and 815 events. Energies of coincident prompt γ rays were corrected for the Doppler shift in the spectra shown in Fig. 3. For the $(p,2p)$ reaction channel, the most intense γ-ray transition was observed at 2,600(33) keV (error, standard deviation, s.d.) with a significance level (S.L.) of 7.5 and tentatively assigned to the $2_1^+ \rightarrow 0_{gs}^+$ decay of ^{78}Ni. Four weaker transitions located at 583(10), 1,103(14), 1,540(25), and 2,110(48) keV were identified. All decay strengths, corrected for the γ-ray-energy dependent detection efficiency of DALI2, and confidence levels, are summarised in Extended Data Table 1 and in Extended Data Fig.2. Sufficient statistics allowed to establish prompt coincidences between the 2,600-keV transition and all the weaker transitions (Fig. 3b), as well as a possible coincidence between the 583-keV transition and the 2,110-keV transition (Extended Data Fig. 1b). Conversely, no coincidence was observed between the 583- and 1,103-keV transitions (Extended Data Fig. 1b,c). They are, therefore, assigned to independently decay into the proposed 2_1^+ state. On account of its correspondence to the theoretical descriptions discussed below, the 583-keV line is tentatively assigned to the $4_1^+ \rightarrow 2_1^+$ transition. This leads to a ratio between the $E(2_1^+)$ and $E(4_1^+)$ of $R_{4/2} = 1.22$, which is comparable to well-known doubly magic nuclei ^{40}Ca (1.35), ^{48}Ca (1.18), ^{56}Ni (1.45), ^{132}Sn (1.09), and ^{208}Pb (1.06).

γ rays from the ^{80}Zn$(p,3p)^{78}$Ni reaction

Although similar amounts of $(p,2p)$ and $(p,3p)$ events were detected, the findings were largely different. A transition remained visible at 1,067(17) keV in the $(p,3p)$ spectrum (Fig. 3d), but no further prominent peak was observed in the energy range up to 2,600 keV, with transitions reported for the $(p,2p)$ channel possessing only S.L. around 1. A surprising additional strength above the $2_1^+ \rightarrow 0_{gs}^+$ decay revealed a transition at 2,910(43) keV with a S.L. of 3.5, which is either weakly or not populated in the $(p,2p)$ channel. It could not be interpreted as a decay into the 2_1^+ state due to the low intensity of the peak at 2,600 keV. Instead, it is ascribed to the decay of a second 2^+ state to the 0^+ ground state. This level placement is further corroborated by the spectrum for γ-ray detection multiplicities of $M_\gamma < 4$ (Fig. 3c), which enhances the peak-to-total ratio of decays from low-lying levels, in this case the 2,910-keV transition. Applying similar arguments to the 1,067-keV transition, its intensity is too large to be identical with the 1,103-keV transition observed in the $(p,2p)$ channel, and is, therefore, placed as feeding the 2,910-keV level. Taking all these observations into account, the level scheme shown in Fig. 4b is proposed for ^{78}Ni.

Doubly magic ^{78}Ni

The $E(2_1^+)$ along the chain of nickel isotopes are presented in Fig. 4a, which exhibit a local maximum at ^{68}Ni that is attributed to the $N = 40$ harmonic oscillator (HO) shell closure. This assessment is reinforced by its low quadrupole collectivity[37]. However, mass measurements identified it as a very localised feature[38] and ref.[39] pointed out that quadrupole collectivity is dominated by neutron excitations. Beyond the HO shell closure, in the independent particle model neutrons fill the $\nu 0g_{9/2}$ SPO with little impact on the $E(2_1^+)$ until a steep rise is observed for our value at $N = 50$. In fact, the 2.6 MeV excitation energy is essentially as high as the 2.7 MeV for the doubly magic ^{56}Ni ($Z = N = 28$)[40], thus providing first direct experimental evidence for a comparable magic character. To gain further insight into the structural evolution of the neutron-rich nickel isotopes, their $E(2_1^+)$ values were confronted with state-of-the-art theoretical calculations in Fig. 4a. Large-scale shell model (LSSM) calculations comprised the two shell-model Hamiltonians outlined in refs.[28,41] with a transition at $N = 44$ from the LNPS to the PFSDG-U Hamiltonian. In particular, LSSM calculations for ^{78}Ni included the full proton pf and neutron sdg HO shells into their model space, which is crucial to pick up emerging quadrupole collectivity from quasi-degenerated neutron SPOs[28].

The Monte Carlo Shell Model (MCSM)[42] allows to incorporate more SPOs into the calculation. For the MCSM predictions presented here, the A3DA-m Hamiltonian[43] was employed for $^{64-76}$Ni, which encompasses the full pf shell as well as the $0g_{9/2}$ and $1d_{5/2}$ SPOs for protons and neutrons. To enable more detailed calculations for ^{78}Ni, the A3DA-m Hamiltonian was extended to the full proton and neutron pf and sdg shells. The mean field based quasi-particle random-phase approximation (QRPA)[44] calculations implemented the Gogny D1M effective force[45]. Finally, we present new *ab initio* results based on the valence-space formulation[46] of the in-medium similarity renormalization group (IM-SRG)[47] and show the coupled-cluster (CC) method[27], both using two- and three-nucleon interactions derived from chiral effective field theory[48]. All theoretical calculations well describe the pattern of $E(2_1^+)$ along the chain of nickel isotopes in Fig. 4a, notably the large enhancement at $N = 50$, thus confirming ^{78}Ni as a doubly magic nucleus.

Two different shapes emerge

Complete predictions for the low-lying level structure of ^{78}Ni are presented in Fig. 4b next to the proposed experimental level scheme. The LSSM and MCSM calculations analogously predict competing spherical (quadrupole deformation parameter, $\beta \sim 0$) and prolate deformed ($\beta \sim 0.3$) intruder configurations, with one discrepancy. While LSSM puts the deformed 2^+ state at 2.88 MeV, and thus below the spherical 2^+ state at 3.15 MeV, for MCSM the deformed 2^+ state at 2.89 MeV lies above the spherical 2^+ state at 2.57 MeV. Respective 4^+ states are located approximately 0.5–0.7 MeV above the 2^+ states, hence justifying the tentative spin assignment for the experimental level at 3.18 MeV. In addition, calculated deformed 0^+ states are located approximately 0.25 MeV below their respective deformed 2^+ states. A possible, unobserved transition from the deformed 2^+ state to the deformed 0^+ state is expected to be several orders of magnitude weaker than direct decays to the ground state due to the large energy difference of the latter. It is further noted that restricting the MCSM calculations to the A3DA-m Hamiltonian[43] puts the first 2^+ state to 2.89 MeV and the second 2^+ state to 4.72 MeV, strikingly demonstrating the necessity for the inclusion of the full neutron sdg shell to properly characterise low-lying deformed configurations[28].

It is important to stress the structural differences between the spherical and deformed configurations, specifically the average number of particle-hole (p-h) excitations above $Z = 28$ ($n_{\text{p-h}}^{\pi}$) and $N = 50$ ($n_{\text{p-h}}^{\nu}$) for the 0^+, 2^+, and 4^+ states. With MCSM, the numbers are $0.4 \lessapprox n_{\text{p-h}}^{\pi} \lessapprox 0.9$ and $0.7 \lessapprox n_{\text{p-h}}^{\nu} \lessapprox 1.7$ for the three spherical states, whilst the respective values are $n_{\text{p-h}}^{\pi} \approx 2.5$ and $n_{\text{p-h}}^{\nu} \approx 2.7$ for the deformed states. Similar values are obtained with LSSM. Recollecting the contrasting levels

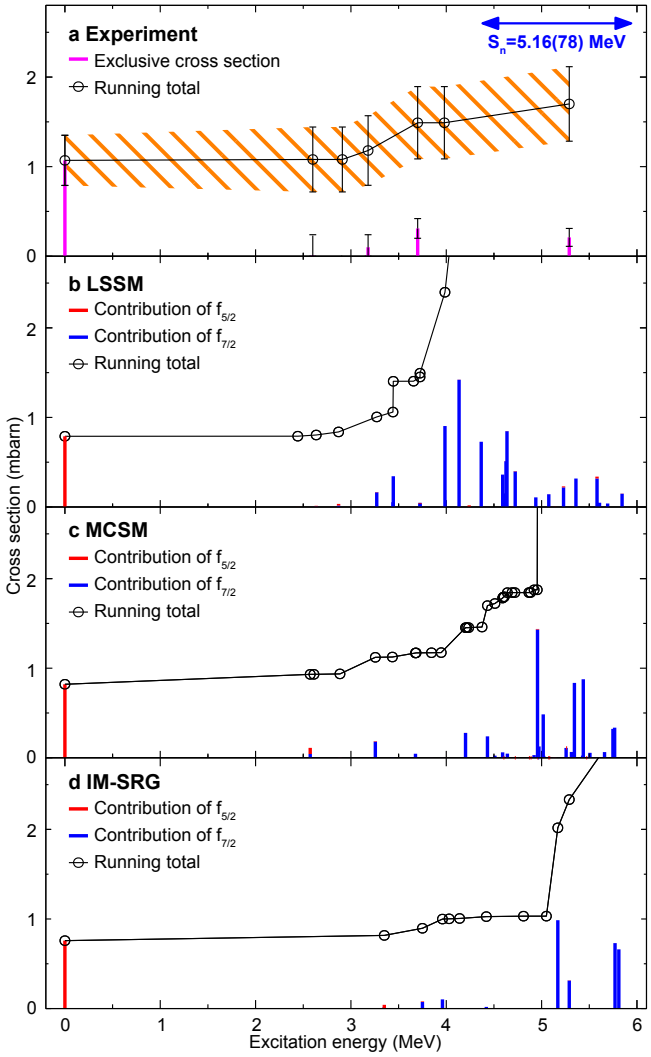

Fig. 5 | Experimental and calculated exclusive cross sections for the ^{79}Cu$(p,2p)^{78}$Ni reaction. **a**, Measured exclusive cross sections (magenta vertical bars). The evaluated neutron separation energy, S_n, and its errors (1 s.d.) are indicated. **b**, Exclusive cross sections predicted by LSSM. **c**, Prediction by MCSM. **d**, Prediction by IM-SRG. In **b**–**d**, contributions of proton removal from $\pi 0f_{5/2}$ and $\pi 0f_{7/2}$ SPOs are distinguished by red and blue vertical bars, respectively. Integrated cross sections are shown as running total function of the excitation energy for the experimental and the theoretical predictions. Contributions from the $\pi 1p_{3/2}$ SPO amount to less than 0.05 mbarn and were omitted. Every circle along the running total corresponds to an observed or calculated level.

populated from $(p,2p)$ and $(p,3p)$ reactions, calculated spectroscopic factors, which quantify the overlap between final and initial state in single nucleon removal reactions, can help unravel the nature of levels populated. Inspection of these spectroscopic factors from ^{79}Cu to final states in ^{78}Ni with the LSSM and MCSM Hamiltonians shows spherical configurations are strongly favoured. Experimental exclusive cross sections to the individual levels are compared in Fig. 5 to calculated ones obtained within the distorted-wave impulse approximation (DWIA) formalism[49] folded with the shell-model spectroscopic factors (see Methods). While the assumptions of the DWIA and shell-model spectroscopic factor calculations are not fully consistent, their combination provides a qualitative picture that can be compared to experiment. Note that for the removal of a single proton in the $\pi 0f_{7/2}$ or $\pi 0f_{5/2}$ SPO, calculated cross sections, which are weakly dependent on projectile and excitation energy, are ~ 1 mbarn. The bulk of spectroscopic strength, which originates from the removal of a $\pi 0f_{7/2}$ proton, is calculated at energies between 4–5 MeV, with an abrupt increase not observed experimentally. However, this energy is close or beyond the evaluated neutron separation energy, S_n, of 5.16(78) MeV[50]. Due to this large uncertainty of S_n, quantitative comparisons between the experimental and theoretical inclusive cross sections were not feasible, but it is noted that LSSM places the average of the distribution lower than MCSM. Good agreement is observed for the ground state, which corresponds predominantly to a removal of a $\pi 0f_{5/2}$ proton, and the strikingly low direct population of the observed low-lying levels, visualised by means of the resembling running totals in Fig. 5. To date, no theoretical framework can predict microscopic $(p,3p)$ cross sections. It must be stressed, however, that the calculated two-nucleon overlaps between the ground state in ^{80}Zn and the excited states in ^{78}Ni also favour the population of spherical final states.

Nickel isotopes represent the neutron-rich frontier for *ab initio* calculations. For the IM-SRG results in Fig. 4b (for details, see Methods), we predict the $E(2_1^+)$ of ^{78}Ni to be 3.35 MeV and the $E(4_1^+)$ at 3.75 MeV with a proton pf and neutron sdg SPO valence-space Hamiltonian. While this is several hundred keV higher than measured, it is nevertheless in good agreement with experimental trends across the chain and also predicts a sharp decrease in $E(2_1^+)$ at ^{80}Ni. Average proton and neutron excitations for the 2_1^+ are $n^{\pi}_{\text{p-h}} = 0.9$ and $n^{\nu}_{\text{p-h}} = 1.3$, analogous to the LSSM and MCSM, and also the exclusive cross sections (Fig. 5d) follow a similar trend. A stark variation is, however, found for the second 2^+ state, which lies at 5.81 MeV and is of spherical nature. This deficiency is not unexpected, as *ab initio* methods are often built on truncations in allowed particle-hole excitations and thus fail to capture very collective features sufficiently. In fact, the $E(2_1^+)$ of ^{78}Ni only varies about 100 keV when using several two- and three-nucleon interactions, so missing particle-hole excitations are likely the main uncertainty of the IM-SRG calculations. In particular, our IM-SRG results agree with the *ab initio* CC predictions of ref.[27] at the level of singles and doubles correlations when using the same Hamiltonian. When triples correlations are

further included, the $E(2_1^+)$ from CC for ^{78}Ni is found to be in good agreement with the present measurement.

In the case of QRPA calculations, 65% of the 2_1^+ wave function of ^{78}Ni is composed of neutron excitations from the $\nu 0g_{9/2}$ to the $\nu 1d_{5/2}$ orbital, across the $N = 50$ shell gap, while 28% are proton excitations from the $\pi 0f_{7/2}$ to the $\pi 0f_{5/2}$ orbitals. In this approach, the neutron shell gap at $N = 50$ is robust enough so that protons across the $Z = 28$ shell gap significantly contribute to the excitation. Similarly, in the neighbouring even-even isotopes ^{76}Ni and ^{80}Ni, the 2_1^+ excitation stems from neutron excitations in the $\nu 0g_{9/2}$ (80% of the wave function) and in the $\nu 1d_{5/2}$ (72% of the wave function with an occupancy of 0.3 neutrons) SPOs, respectively.

In conclusion, first direct experimental evidence for the preservation of the $Z = 28$ and $N = 50$ shell closures in ^{78}Ni was provided by employing a dedicated set-up to study extremely exotic nuclei via in-beam γ-ray spectroscopy. A low-lying, second 2^+ state conforms with the notion of competing spherical and deformed configurations, which is to be verified by future measurements in ^{76}Fe and ^{74}Cr[28]. Similarly, a breakdown of the proton $Z = 28$ shell closure that favours prolate deformed ground states for heavier nickel isotopes is predicted, establishing ^{78}Ni as doubly magic stronghold before deformation prevails in more exotic nuclei. Understanding these structures is crucial for r-process nucleosynthesis, as the onset of deformation may shift the drip line towards heavier isotopes. Driving mechanisms for this evolution from spherical to deformed nuclei are yet to be fully understood at the *ab initio* level, prompting also future mass measurements to validate the predicted collapse of traditional shell closures.

References

1. Wienholtz, F. *et al.* Masses of exotic calcium isotopes pin down nuclear forces, Nature **498**, 346-349 (2013).
2. Steppenbeck, D. *et al.* Evidence for a new nuclear "magic number" from the level structure of ^{54}Ca, Nature **502**, 207-210 (2013).
3. Erler, J. *et al.* The limits of the nuclear landscape, Nature **486**, 509-512 (2012).
4. Haxel, O., Jensen, J. & Suess, H. On the "Magic Numbers" in Nuclear Structure, Phys. Rev. **75**, 1766 (1949).
5. Goeppert Mayer, M. On Closed Shells in Nuclei, Phys. Rev. **75**, 1969 (1949).
6. Navin, A. *et al.* Direct evidence of the breakdown of the $N = 8$ shell closure in ^{12}Be, Phys. Rev. Lett. **85**, 266-269 (2000).
7. Thibault, C. *et al.* Direct measurement of the mass of ^{11}Li and $^{26\text{-}31}$Na with an on-line mass separator, Phys. Rev. C **12**, 644-657 (1975).
8. Guillemaud-Mueller, D. *et al.* β decay schemes of very neutron-rich sodium isotopes and their descendants, Nucl. Phys. A **426**, 37-76 (1984).
9. Bastin, B. *et al.* Collapse of the $N = 28$ shell closure in ^{42}Si, Phys. Rev. Lett. **99**, 022503 (2007).
10. Tshoo, K. *et al.* $N = 16$ spherical shell closure in ^{24}O, Phys. Rev. Lett. **109**, 022501 (2012).
11. Huck, A. *et al.* Beta decay of the new isotopes ^{52}K, ^{52}Ca, and ^{52}Sc; a test of the shell model far from stability, Phys. Rev. C **31**, 2226-2237 (1985).
12. Talmi, I. & Unna, I. Order of Levels in the Shell Model and Spin of ^{11}Be, Phys. Rev. Lett. **4**, 469-470 (1960).
13. Otsuka, T., Suzuki, T., Fujimoto, R., Grawe, H. & Akaishi, Y. Evolution of the nuclear shells due to the tensor force, Phys. Rev. Lett. **95**, 232502 (2005).
14. Otsuka, T. *et al.* Novel features of nuclear forces and shell evolution in exotic nuclei, Phys. Rev. Lett. **104**, 012501 (2010).
15. Otsuka, T., Suzuki, T., Holt, J.D., Schwenk, A. & Akaishi, Y. Three-Body Forces and the Limit of Oxygen Isotopes, Phys. Rev. Lett. **105**, 032501 (2010).
16. Hammer, H.-W., Nogga, A. & Schwenk, A. Three-body forces: From cold atoms to nuclei, Rev. Mod. Phys. **85**, 197-217 (2013).
17. Engelmann, Ch. *et al.* Production and identification of heavy Ni isotopes: evidence for the doubly magic nucleus $^{78}_{28}$Ni, Z. Phys. A **352**, 351-352 (1995).
18. Van de Walle, J. *et al.* Coulomb excitation of neutron-rich Zn isotopes: first observation of th 2_1^+ state in ^{80}Zn, Phys. Rev. Lett. **99**, 142501 (2007).
19. Hakala, J. *et al.* Evolution of the $N = 50$ shell gap energy towards ^{78}Ni, Phys. Rev. Lett. **101**, 052502 (2008).
20. Mazzocchi, C. *et al.* Low energy structure of even-even Ni isotopes close to ^{78}Ni, Phys. Lett. B **622**, 45-54 (2000).
21. Hosmer, P.T. *et al.* Half-life of the doubly magic r-process nucleus ^{78}Ni, Phys. Rev. Lett. **94**, 112501 (2005).
22. Xu, Z.Y. *et al.* β-decay half-lives of ^{76,77}Co, ^{79,80}Ni and ^{81}Cu: Experimental indication of a doubly magic ^{78}Ni, Phys. Rev. Lett. **113**, 032505 (2014).
23. Sahin, E. *et al.* Shell evolution towards ^{78}Ni: Low-lying States in ^{77}Cu, Phys. Rev. Lett. **118**, 242502 (2017).
24. Olivier, L. *et al.* Persistence of the $Z = 28$ shell gap around ^{78}Ni: First spectroscopy of ^{79}Cu, Phys. Rev. Lett. **119**, 192501 (2017).
25. Welker, A. *et al.* Binding Energy of ^{79}Cu: Probing the Structure of the Doubly Magic ^{78}Ni from Only One Proton Away, Phys. Rev. Lett. **119**, 192502 (2017).
26. Santamaria, C. *et al.* Extension of the $N = 40$ Island of Inversion towards $N = 50$: Spectroscopy of ^{66}Cr, ^{70,72}Fe, Phys. Rev. Lett. **115**, 192501 (2015).
27. Hagen, G., Jansen, G. R. & Papenbrock, T. Structure of ^{78}Ni from First-Principles Computations, Phys. Rev. Lett. **117**, 172501 (2016).
28. Nowacki, F., Poves, A., Caurier, E. & Bounthong, B. Shape Coexistence in ^{78}Ni as the Portal to the Fifth Island of Inversion, Phys. Rev. Lett. **117**, 272501 (2016).
29. Franchoo, S. *et al.* Beta-Decay of $^{68\text{–}74}$Ni and Level Structure of Neutron-Rich Cu Isotopes, Phys. Rev. Lett. **81**, 3100-3103 (1998).
30. Flanagan, K.T. *et al.* Nuclear Spins and Magnetic Moments of ^{71,73,75}Cu: Inversion of $\pi 2p_{3/2}$ and $\pi 1f_{5/2}$ Levels in ^{75}Cu, Phys. Rev. Lett. **103**, 142501 (2009).
31. Sieja, K. & Nowacki F. Shell quenching in ^{78}Ni: hint from the structure of neutron-rich copper isotopes, Phys. Rev. C **81**, 061303(R) (2010).
32. Gottardo, A. *et al.* First Evidence of Shape Coexistence in the ^{78}Ni Region: Intruder 0_2^+ State in ^{80}Ge, Phys. Rev. Lett. **116**, 182501 (2016).

33. Yang, X.F. *et al.* Isomer Shift and Magnetic Moment of the Long-Lived $1/2^+$ Isomer in $^{79}_{30}Zn_{49}$: Signature of Shape Coexistence near ^{78}Ni, Phys. Rev. Lett. **116**, 182502 (2016).
34. Kubo, T. *et al.* BigRIPS separator and ZeroDegree spectrometer at RIKEN RI Beam Factory, Prog. Theo. Phys. **2012**, 03C003 (2012).
35. Obertelli, A. *et al.* MINOS: A vertex tracker coupled to a thick liquid-hydrogen target for in-beam spectroscopy of exotic nuclei, Eur. Phys. J. A **50**, 8 (2014).
36. Takeuchi, S. *et al.* DALI2: A NaI(Tl) detector array for measurements of γ rays from fast nuclei, Nucl. Instr. and Meth. in Phys. Res. A **763**, 596-603 (2014).
37. Sorlin, O. *et al.* ^{68}Ni: Magicity versus Superfluidity, Phys. Rev. Lett. **88**, 092501 (2002).
38. Guénaut, C. *et al.* High-precision mass measurements of nickel, copper, and gallium isotopes and the purported shell closure at $N = 40$, Phys. Rev. C **75**, 044303 (2007).
39. Langanke, K., Terasaki, J., Nowacki, F., Dean, D.J. & Nazarewicz, W. How magic is the magic ^{68}Ni nucleus?, Phys. Rev. **67**, 044314 (2003).
40. National Nuclear Data Center. Evaluated Nuclear Structure Data File. http://www.nndc.bnl.gov/ensdf/ (2018).
41. Lenzi, S.M., Nowacki, F., Poves, A. & Sieja, K. Island of inversion around ^{64}Cr, Phys. Rev. C **82**, 054301 (2010).
42. Shimizu, N. *et al.* New-generation Monte Carlo shell model for the K computer era, Prog. Theor. Exp. Phys. **2012**, 01A205 (2012).
43. Tsunoda, Y., Otsuka, T., Shimizu, N., Honma, M. & Utsuno, Y. Novel shape evolution in exotic Ni isotopes and configuration-dependent shell structure, Phys. Rev. C **89**, 031301(R) (2014).
44. Péru, S. & Martini, M. Mean field based calculations with the Gogny force: Some theoretical tools to explore the nuclear structure, Eur. Phys. J. A **40**, 88 (2014).
45. Goriely, S., Hilaire, S., Girod, M. & Péru, S. First Gogny-Hartree-Fock-Bogoliubov Nuclear Mass Model, Phys. Rev. Lett. **102**, 242501 (2009).
46. Stroberg, S.R. *et al.* Nucleus-Dependent Valence-Space Approach to Nuclear Structure, Phys. Rev. Lett. **118**, 032502 (2017).
47. Hergert, H., Bogner, S. K., Morris, T. D., Schwenk, A. & Tsukiyama, K. The In-Medium Similarity Renormalization Group: A novel *ab initio* method for nuclei, Phys. Rep. **621**, 165-222 (2016).
48. Epelbaum, E., Hammer, H.-W. & Meißner, Ulf-G. Modern theory of nuclear forces, Rev. Mod. Phys. **81**, 1773-1825 (2009).
49. Wakasa, T., Ogata, K. & Noro, T. Proton-induced knockout reactions with polarized and unpolarized beams, Prog. Part. Nucl. Phys. **96**, 32-87 (2017).
50. Wang, M. *et al.* The AME2016 atomic mass evaluation, Chinese Physics C **41**, 030003 (2017).

Acknowledgements

We express our gratitude to staff of the RIKEN Nishina Center accelerator complex for providing the stable and high-intensity uranium beam, and to the BigRIPS team for the smooth operation of the secondary beams. We also thank for contributions by Mr. Narumasa Miyauchi for providing us the 3D schematic figure of the RIBF facility shown in Fig. 2a. The development of MINOS and the core MINOS team have been supported by the European Research Council through the ERC Grant No. MINOS-258567. R.T. was supported by JSPS Grant-in-Aid for JSPS Research Fellow Grant Number JP14J08718. A.O. was supported by JSPS long-term fellowship L-13520 at the RIKEN Nishina Center. C.Sa. was supported by the IPA program at the RIKEN Nishina Center. J.D.H acknowledges the support by National Research Council of Canada and NSERC. This work was supported in part by the ERC Grant No. 307986 STRONGINT, the DFG under Grant SFB 1245, and the BMBF under Contract No. 05P18RDFN1. The MCSM calculations were performed on K computer at RIKEN AICS (hp160211, hp170230, hp180179). J.M., T.O., and Y.T. acknowledge the support from MEXT as "Priority Issue on post-K computer" (Elucidation of the Fundamental Laws and Evolution of the Universe) and JICFuS. J.M. and K.O. were supported by Grant-in-Aid for Scientific Research JP18K03639 (J.M.) and JP16K05352 (K.O.). A.Po. acknowledges the support by Mineco (Spain) grants FPA2014-57916 and Severo Ochoa Program SEV-2016-0597. This work was supported in part by the DFG through the Cluster of Excellence PRISMA. L.X.C. was supported by the Vietnam MOST through the Physics Development Program Grant No. ĐTĐLCN.25/18. Zs.D., Z.K., and Zs.V. acknowledge the support from the GINOP-2.3.3-15-2016-00034 project. M.L, C.L, and V.W. acknowledge the support from the German BMBF Grants No. 05P15RDNF1, No. 05P12RDNF8.

Author contributions

R.T. performed offline data analyses and GEANT4 simulations, and prepared the figures; P.D., and A.O. designed the experiment; R.T., C.Sa., P.D., A.O., J.D.H., J.M., F.N., K.O., T.O., A.S., and Y.T. wrote the manuscript; R.T., C.Sa., P.D., A.O., G.A., D.C., F.C., A.C., A.D., J.-M.G, A.G., V.L., M.M., S.M., M.N., C.P,. A.Pe., E.C.P., J.-Y.R., Y.S., S.T., and H.W. were responsible for setting up the liquid hydrogen target and vertex reconstruction system, MINOS, and the γ-ray detector array, DALI2; R.T., C.Sa., H.B., D.C., A.C., and T.I. were responsible for the data acquisition system and analysis software; R.T., C.Sa., P.D., A.O., G.A., H.B., D.C., F.C., A.C., A.D., J.-M.G, A.G., T.I., V.L., M.M., S.M., M.N., H.O., C.P., A.Pe., E.C.P., J.-Y.R., Y.S., S.T., H.W., F.B., L.X.C., Zs.D., S.F., F.G., A.G., K.H., Z.K., S.K., J.L., M.L., C.L., R.L., K.N., T.Mi., S.N., L.O., S.O., Z.P., E.S., C.Sh., P.-A.S., I.S., D.St., T.S., D.Su, Zs.V, V.W., J.W., and Z.Y.X. checked data accumulation online and maintained operation of the ex-

periment; P.D., A.O., K.Y., T.Mo., H.S., and T.U. supervised the participants; F.N. and A.Po. performed the LSSM calculations; T.O. and Y.T. performed the MCSM calculations; S.P. performed the QRPA calculations; J.D.H., J.M., A.S., J.S., and S.R.S. performed the IM-SRG calculations; K.O. performed the DWIA calculations; All authors discussed the results and commented on the manuscript.

Additional information

Reprints and permissions information is available at www.nature.com/reprints.
Competing interests The authors declare no competing interests.
Correspondence and requests for materials should be addressed to P.D.

Methods

Beam production. The experiment was performed at the Radioactive Isotope Beam Factory, Japan, operated by the RIKEN Nishina Center and the Center for Nuclear Study of the University of Tokyo. A ^{238}U primary beam with an intensity of 7.5×10^{10} p.p.s. was accelerated by four coupled cyclotrons[51] to an energy of 345 MeV/u and impinged on a 3-mm-thick beryllium production target, located at the F0 focus of the BigRIPS two-stage fragment separator[34] shown in Fig. 2a. The isotopes of interest were first purified with the BigRIPS fragment separator from focal plane F0 to F2 by their magnetic rigidity and energy loss. Particles then traversed BigRIPS from F3 to F7 at approximately 60% of the speed of light and were identified by time-of-flight, magnetic rigidity, and energy loss measurements on an event-by-event basis[52,53]. Secondary beam rates of 5 p.p.s. for ^{79}Cu and 290 p.p.s. for ^{80}Zn were directed onto the MINOS reaction target system.

Secondary reaction. MINOS[35] consisted of a tube of 102(1)-mm length and 38-mm inner diameter filled with liquid hydrogen coupled with a time projection chamber (TPC). Secondary reaction products were selected and identified with the ZeroDegree spectrometer following the same approach as for BigRIPS. Emitted prompt γ rays were detected with DALI2[36], which consisted of 186 NaI(Tl) scintillators arranged in a geometry that covered polar angles from 12 to 96 degrees surrounding the MINOS system and achieved a photo-peak efficiency of 26% at 1 MeV. Figure 2b shows the schematic view of DALI2 and MINOS. Around 30% energy loss inside the secondary target resulted in a highly reaction vertex position dependent velocity. Therefore, an annular TPC surrounded the cryogenic target to determine the vertex position following $(p, 2p)$ and $(p, 3p)$ removal reactions.

Data acquisition. The general data acquisition system at the RIBF facility[53] was coupled with the dedicated MINOS electronics system[54,55] developed to readout the roughly 5,000 channels comprising the pad plane of the TPC.

Vertex tracking and γ-ray energy reconstruction. Observed γ-ray energies in the laboratory system were reconstructed for their Doppler shift, as described in ref.[56]. For this reconstruction, the vertex position was determined with the TPC by tracking the protons in the $(p, 2p)$ and $(p, 3p)$ knockout reactions of interest via an iterative tracking algorithm using a Hough transform method, detailed in ref.[57]. This process allowed a vertex resolution of less than 5 mm full width at half maximum. The velocity at incident point was determined assuming energy loss inside the liquid hydrogen target according to the ATIMA code (https://web-docs.gsi.de/∼weick/atima/).

Compton scattering of γ rays resulted in partial energy deposition between neighbouring crystals of DALI2. In the case γ rays were observed in detectors within a 15-cm distance, the energy was summed and the detector with highest energy determined the position for the Doppler reconstruction.

The γ-ray detector response functions were simulated with the GEANT4 framework[58] for fitting and comparison with the experimental data.

Stationary sources of ^{60}Co, ^{88}Y, and ^{137}Cs provided γ-ray energies to calibrate the array.

Energy reconstruction of peaks. Five and six peak candidates were investigated in the $(p, 2p)$ and $(p, 3p)$ channels, respectively. The energy values and their corresponding errors and intensities were determined by maximising the likelihood values of the fits of 10 keV binned spectra with all combinations of transition energies assuming a multivariate Gaussian probability density function. The S.L. for the existence of each peak was deduced from the probability value of the likelihood ratio between the null hypothesis and the alternative hypothesis. Obtained results are summarised in Extended Data Table 1 and in Extended Data Fig.2.

LSSM calculation. Following ref.[28], Large Scale Shell-Model Calculations were carried out in a valence space comprising the pf shell orbitals for protons and the sdg shell orbitals for neutrons, with an effective interaction based on realistic matrix elements for which the monopole part was adjusted to reproduce the experimental evolution of the regulating gaps in the model space. Besides the convincing spectroscopy exhibited in the comparison panels of Fig. 4, the spectroscopic qualities of this interaction was already assessed in the recent studies in the region[25,59–62]. In order to generate the theoretical spectroscopic strength of one proton removal from ^{79}Cu to final states in ^{78}Ni, the Lanczos Strength Function Method[63,64] was applied to LSSM calculations. In practice, the removal operator was applied on the initial ^{79}Cu ground state to generate the sum rule state $\Sigma = \tilde{a}_j \left| \frac{5}{2}^- \right\rangle$. This non physical state carried the entire one proton removal spectroscopic strength and was used as the initial state for a Lanczos diagonalisation procedure. At the end of the procedure, the matrix elements were simply the components of Σ in the Lanczos eigenstates basis. Even if the diagonalisation was not fully complete; this procedure converged rapidly to an approximate strength distribution. To handle more easily the large dimension of the involved basis without losing any physics insight, the proton and neutron gaps were slightly reduced to project the results of ref.[28] into a smaller valence space containing all excitations across the $Z = 28$ and $N = 50$ up to 7 particle-hole excitations. We checked that the orbital occupancies for ^{78}Ni low-lying states and ^{79}Cu ground-state wave functions remained identical to the ones obtained in the configuration space of ref.[28].

MCSM calculation. The MCSM calculation is one of the most advanced computational methods that can be

applied for nuclear many-body systems. This work represents the MCSM calculations performed on the K computer at RIKEN AICS, Japan. Exploiting the advantages of quantum Monte Carlo variational and matrix-diagonalisation methods, this approach circumvents the diagonalisation of a $> 5 \times 10^{20}$-dimensional Hamiltonian matrix. Using the doubly magic ^{40}Ca nucleus as an inert core, 8 protons and up to 32 neutrons were left to actively interact in a much larger model space as compared to conventional configuration interaction calculations. The A3DA-m interaction[43] in the model space of 6 SPOs (pf shell, $0g_{9/2}$ and $1d_{5/2}$ orbitals) both for protons and neutrons was used for $^{64\text{-}76}$Ni. This interaction was extended to a model space of 9 SPOs (pf and sdg shells) for ^{78,80}Ni where upper SPOs in the sdg shell become more important. The MCSM eigenstate is represented as a superposition of MCSM basis vectors with the appropriate projection onto spin and parity. Each MCSM basis vector is a Slater determinant formed by mixed single-particle states, where the mixing amplitudes are optimised by quantum Monte Carlo and variational methods. This Slater determinant has intrinsic quadrupole moments, which can be expressed in terms of a set of β_2 and γ deformation parameters. This property can be used to study the intrinsic shape of the calculated state.

The MCSM calculations with the A3DA-m interaction reveal properties of Ni and neighbouring isotopes. Shape evolution of nickel isotopes including shape coexistence has been described theoretically[43] and the calculations have been compared with experiments for ^{66}Ni[65], ^{68}Ni[66,67], and ^{70}Ni[68,69]. Nuclei near $N = 50$ have been described well by the calculations for ^{77}Cu[23] and ^{79}Cu[24].

In-medium similarity renormalization group. The in-medium similarity renormalization group (IM-SRG)[47,70] transforms the many-body Hamiltonian, H, to a diagonal or block-diagonal form, $\tilde{H} = UHU^\dagger$, via a unitary transformation, $U = e^\Omega$, where the anti-Hermitian generator, Ω, builds in the off-diagonal correlations from the original H[71]. The IM-SRG starts from a single-reference ground-state configuration, $|\Phi_0\rangle$ (such as Hartree-Fock), at the flow parameter, $s = 0$, and connects this state to the fully correlated ground state, $|\Psi_0\rangle$, as $s \to \infty$, where the unitary transformation is also built up as a continuous sequence of unitary transformations, $U(s)$. With no truncations in the IM-SRG flow equations, this gives the exact ground-state energy, but in the IM-SRG(2) approximation used here, all operators are truncated at the two-body level. In the valence-space IM-SRG formulation[46,72–74], the unitary transformation is constructed to in addition decouple the valence space, leading to a valence-space Hamiltonian, which is subsequently diagonalised within the valence space using large-scale shell-model methods. In this work, this encompasses a ^{60}Ca core and a Hamiltonian composed of the proton pf and neutron sdg SPOs.

Here, we used a particular set of two- and three-nucleon interactions (labelled 1.8/2.0 (EM)[75]), which was fit in few-body systems, but predicts ground state energies very well to ^{100}Sn[76]. The calculations adequately reproduce the $E(2_1^+)$ trend from ^{70}Ni to the steep rise in excitation energy for ^{78}Ni. In addition, the 1.8/2.0 (EM) interaction within the IM-SRG framework systematically predicts experimental binding energies and $E(2_1^+)$ of lighter nuclei up to the nickel isotopes, including high $E(2_1^+)$ values at known shell closures[77]. As for LSSM, spectroscopic factors were obtained with the Lanczos method[63].

The shell model diagonalisation of nickel isotopes up to ^{72}Ni is exact in the valence space. Due to exceeding dimensions, for ^{74}Ni and ^{78}Ni, the number of particle-hole excitations across the proton $f_{7/2}$ orbital ($Z = 28$) and the neutron $g_{9/2}$ orbital is limited to $7p$-$7h$. Similarly, for ^{76}Ni and ^{80}Ni up to $6p$-$6h$ and $5p$-$5h$ excitations were included, respectively. The convergence of the results in terms of np-nh excitations suggests uncertainties of about 10 keV for ^{74,76}Ni and 50 keV for ^{78,80}Ni. The spectroscopic factors shown if Fig. 5d are calculated diagonalising ^{79}Cu including up to $6p$-$6h$ excitations. At this level, the convergence of the largest spectroscopic factors is better than 5 %. Thus, these uncertainties are smaller than the uncertainties from the input two- and three-nucleon interactions as well as the IM-SRG truncations.

QRPA calculation. In the presented QRPA approach, the second-order matrix was fully diagonalised[44,78], in agreement with the variational principle applied in Hartree-Fock-Bogoliubov (HFB) mean field calculations. Eigenvalues and eigenvectors provided excitation energies and wave functions for all vibrational excited states described as coherent states of two quasi-particle excitations above the ground state. Transition probabilities from the ground state to all described excited states could be calculated for all parities and multipolarities, and for any intrinsic deformation of the ground state. Not only spherical, but also axially-symmetric deformed shapes were considered. QRPA and underlying HFB equations were solved in a finite HO basis with cylindrical coordinates including eleven major shells. In order to preserve symmetry restoration, the same curvature of the HO was given for the both radial and symmetric axis directions. This curvature was chosen for each calculated nucleus in order to minimise the HFB binding energy: The oscillator parameter, $\hbar\omega$, as defined in a previous study[79], was found to be 9.9 MeV for ^{78}Ni.

All HFB quasi-particle states were used to generate the two-quasi-particle excitation set. This means that no additional cut in energy, occupation probabilities nor isospin was introduced. The same effective interaction, namely the D1M parameter set[45] of the Gogny analytical form, was used to solve both the HFB and the QRPA equations in all ph, pp, and hh channels. Since the D1M

effective interaction has been fit without exchange and pairing parts of the Coulomb interaction, only the direct term of the Coulomb field is included in the HFB as well as in QRPA matrix elements. As concluded in a previous study[80], this term should have an impact only in case of large proton pairing energy, which is not the case here where the $Z = 28$ is a closed proton shell. The two-body centre-of-mass correction term was also neglected in the present study, as its impact is expected to be very small.

The QRPA approach provides good agreement with the experimental $E(2_1^+)$, as shown in Fig. 4. Note that the $E(2_1^+)$ of ^{64}Ni has been omitted, as its spherical shape is degenerated with an oblate deformation (see Fig. 42 of ref.[44]) and therefore not suitable for QRPA calculations.

DWIA calculation. DWIA describes a $(p, 2p)$ process as a proton-proton (pp) scattering inside a target nucleus, A. The transition amplitude, T, whose absolute square is proportional to the reaction probability, is given by,

$$T = \langle \chi_1 \chi_2 \left| v \right| \chi_0 \phi_N \rangle \,,$$

where χ represents the scattering waves of the incoming nucleon (χ_0) and the outgoing two nucleons (χ_1 and χ_2), ϕ_N is a bound-state wave function of a nucleon to be knocked out, and v is the pp interaction that causes the $(p, 2p)$ transition. In the plane-wave limit, T becomes a product of the Fourier transforms of v and ϕ_N, which allows one to interpret a $(p, 2p)$ cross section as a snapshot of the momentum distribution of the struck proton inside A. In reality, distortion effects such as deflection and absorption exist, which are well under control by using distorted waves for the incoming proton and outgoing protons. $(p, 2p)$ reactions have been established as an alternative to $(e, e'p)$ reactions. More details can be found in ref.[49].

In the present work, we constructed each χ by a microscopic G-matrix folding model calculation, that is, the pp interaction in infinite nuclear matter was folded by a nuclear density of A. We adopted the Melbourne G-matrix[81] for the former and the Bohr-Mottelson (BM) density[82] for the latter. The microscopic p-A potential was shown to describe proton scattering observables for various nuclei in a very wide range of energies[81]. The BM parameter was used also for ϕ_N. The correction to the nonlocality of χ and ϕ_N was accounted for by the prescription proposed by Perey and Buck[83]. As for the transition interaction v, the Franey-Love parametrisation[84] was employed. All the central, spin-orbit, and tensor parts were included. In Fig. 5, spectroscopic strengths from more deeply bound SPOs are not illustrated as they are negligibly small.

Data availability

All of the relevant data that support the findings of this study are available from the corresponding author upon reasonable request.

References

51. Okuno, H., Fukunishi, N. & Kamigaito, O. Progress of RIBF accelerators, Prog. Theor. Exp. Phys. **2012**, 03C002 (2012).
52. Fukuda, N. *et al.* Identification and separation of radioactive isotope beams by the BigRIPS separator at the RIKEN RI Beam Factory, Nucl. Instr. and Meth. in Phys. Res. B **317**, 323-332 (2013).
53. Baba, H. *et al.* New data acquisition system for the RIKEN Radioactive Isotope Beam Factory, Nucl. Instr. and Meth. in Phys. Res. A **616** 65-68 (2010).
54. Calvet, D. A versatile readout system for small to medium scale gaseous and silicon detectors, IEEE Trans. Nucl. Sci. **61**, 675-682 (2014).
55. Baron, P. *et al.* Operational Experience With the Readout System of the MINOS Vertex Tracker, IEEE Trans. Nucl. Sci. **64** 1494-1500 (2017).
56. Doornenbal, P. In-beam gamma-ray spectroscopy at the RIBF, Prog. Theo. Phys. **2012**, 03C004 (2012).
57. Santamaria, C. *et al.* Tracking with the MINOS Time Projection Chamber, Nucl. Instr. and Meth. in Phys. Res. A **905**, 138-148 (2018).
58. Agostinelli, S. *et al.* GEANT4 – A simulation Toolkit, Nucl. Instr. and Meth. in Phys. Res. A **506**, 250-303 (2003).
59. Wraith, C. *et al.* Evolution of nuclear structure in neutron-rich odd-Zn isotopes and isomers, Phys. Lett. B **771**, 385-391 (2017).
60. De Groote, R.P. *et al.* Dipole and quadrupole moments of $^{73\text{-}78}$Cu as a test of the robustness of the $Z = 28$ shell closure near ^{78}Ni, Phys. Rev. C **96**, 041312(R) (2017).
61. Shand, C.M. *et al.* Shell Evolution Beyond $Z = 28$ and $N = 50$: Spectroscopy of ^{81,82,83,84}Zn, Phys. Lett. B **773**, 492-497 (2017).
62. Cortés, M.L. *et al.* Inelastic scattering of neutron-rich Ni and Zn isotopes off a proton target, Phys. Rev. C **97**, 044315 (2018).
63. Whitehead, R.R. Moment Methods and Lanczos Methods. in *Theory and Applications of Moments Methods in Many Fermion Systems*, edited by Dalton, B.J., Grimes, S.M., Vary, J.D. & Williams, S. A. (Plenum, New York), p.235, (1980).
64. Caurier, E., Martínez-Pinedo, G., Nowacki, F., Poves, A. & Zuker, A.P. The shell model as a unified view of nuclear structure, Rev. Mod. Phys. **77**, 427-488 (2005).
65. Leoni, S. *et al.* Multifaceted Quadruplet of Low-Lying Spin-Zero States in ^{66}Ni: Emergence of Shape Isomerism in Light Nuclei, Phys. Rev. Lett. **118**, 162502 (2017).
66. Suchyta, S. *et al.* Shape coexistence in ^{68}Ni, Phys. Rev. C **89**, 021301(R) (2014).
67. Flavigny, F. *et al.* Characterization of the low-lying 0^+ and 2^+ states in ^{68}Ni via β decay of the low-spin ^{68}Co isomer, Phys. Rev. C **91**, 034310 (2015).
68. Chiara, C. J. *et al.* Identification of deformed intruder states in semi-magic ^{70}Ni, Phys. Rev. C **91**, 044309 (2015).
69. Morales, A.I. *et al.* Type II shell evolution in $A = 70$ isobars from the $N \geq 40$ island of inversion, Phys. Lett. B **765**, 328-333 (2017).

70. Tsukiyama, K., Bogner, S. K. & Schwenk, A. In-Medium Similarity Renormalization Group For Nuclei, Phys. Rev. Lett. **106**, 222502 (2011).
71. Morris, T.D., Parzuchowski, N.M. & Bogner, S.K. Magnus expansion and in-medium similarity renormalization group, Phys. Rev. C **92**, 034331 (2015).
72. Tsukiyama, K., Bogner, S.K. & Schwenk, A. In-medium similarity renormalization group for open-shell nuclei, Phys. Rev. C **85**, 061304(R) (2012).
73. Bogner, S. K. *et al.* Nonperturbative Shell-Model Interactions from the In-Medium Similarity Renormalization Group, Phys. Rev. Lett. **113**, 142501 (2014).
74. Stroberg, S.R., Hergert, H., Holt, J.D., Bogner, S.K. & Schwenk, A. Ground and excited states of doubly open-shell nuclei from ab initio valence-space Hamiltonians, Phys. Rev. C **93**, 051301(R) (2016).
75. Hebeler, K., Bogner, S.K., Furnstahl, R.J., Nogga, A. & Schwenk, A. Improved nuclear matter calculations from chiral low-momentum interactions, Phys. Rev. C **83**, 031301(R) (2011).
76. Morris, T.D. *et al.* Structure of the Lightest Tin Isotopes, Phys. Rev. Lett. **120**, 152503 (2018).
77. Simonis, J., Stroberg, S.R., Hebeler, K., Holt, J.D., Schwenk, A. & Simonis J. Saturation with chiral interactions and consequences for finite nuclei, Phys. Rev. C **96**, 014303 (2017).
78. Péru, S. & Goutte, H. Role of deformation on giant resonances within the quasiparticle random-phase approximation and the Gogny force, Phys. Rev. C **77**, 044313 (2008).
79. Gaudefroy, L. *et al.* Collective structure of the $N = 40$ isotones, Phys. Rev. C **80**, 064313 (2009).
80. Anguiano, M., Egido, J.L. & Robledo, L.M. Coulomb exchange and pairing contributions in nuclear Hartree-Fock-Bogoliubov calculations with the Gogny force, Nucl. Phys. A **683**, 227-254 (2001).
81. Amos, K., Dortmans, P.J., von Geramb, H.V., Karataglidis, S. & Raynal, J. Nucleon-Nucleus Scattering: A Microscopic Nonrelativistic Approach in *Advanced Nuclear Physics*, edited by Negele, J.W. & Vogt, E. (Plenum, New York, 2000), Vol. **25**, p.275.
82. Bohr, A. & Mottelson, B.R. Nuclear Structure (Benjamin, New York, 1969), Vol. I.
83. Perey, F.G. & Buck, B. A non-local potential model for the scattering of neutrons by nuclei, Nucl. Phys. **32**, 353-380 (1962).
84. Franey, M.A. & Love, W.G. Nucleon-nucleon t-matrix interaction for scattering at intermediate energies, Phys. Rev. C **31**, 488-498 (1985).

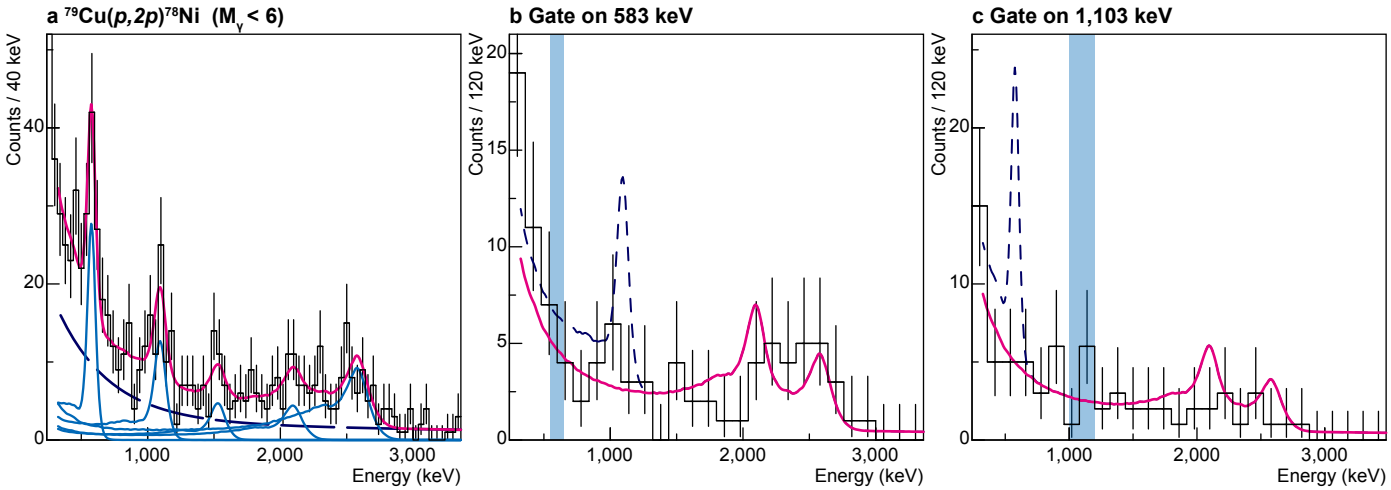

Extended Data Fig. 1 | Energy spectra of prompt γ-ray coincidences with ^{79}Cu$(p, 2p)^{78}$Ni reactions. **a**, Same as Fig. 3a with a binning condition of 40 keV, allowing to resolve the transition at 583 keV. **b**, γ-ray spectrum in coincidence with the 583-keV transition. Expected intensities for coincidences with the 583-keV transition are indicated by the simulated lineshapes, with and without the 1,103-keV transition shown by blue dashed and magenta solid lines, respectively. It reveals of no coincidence between the 583- and 1,103-keV transitions. **c**, γ-ray spectrum in coincidence with the 1,103-keV transition. The hypothesis of no coincidence between the 583- and 1,103-keV transitions is corroborated. Coincidence ranges are illustrated by the hatched area in the respective spectra in **b** and **c**.

Extended Data Table 1 | Observed γ-ray transition energies, relative intensities, and significance levels for the ^{79}Cu$(p, 2p)^{78}$Ni and ^{80}Zn$(p, 3p)^{78}$Ni reaction channels.

Reaction	E_γ (keV)	I_{rel} (%)	Signif cance level
^{79}Cu(p, 2p)^{78}Ni	583(10)	49(11)	5.3 σ
	1,103(14)	49(12)	4.3 σ
	1,540(25)	28(11)	2.6 σ
	2,110(48)	33(13)	2.9 σ
	2,600(33)	100(15)	7.5 σ
	2,910(43)*	—	1.2 σ
^{80}Zn(p, 3p)^{78}Ni	581(16)	46(19)	1.8 σ
	1,067(17)	84(26)	3.5 σ
	1,610(240)	25(23)	1.2 σ
	2,000(40)	66(25)	1.4 σ
	2,720(240)†	48(30)	1.4 σ
	2,910(43)†	100(29)	3.7 σ

De-excitation energies, E_γ, with statistical errors (1 s.d.) determined by maximising likelihoods in probability density functions and the relative intensity, I_{rel}, to the most intense transition for each reaction, are listed. Shown are the significance levels for γ-ray detection multiplicity $M_\gamma < 6$

*The significance level was tested with the obtained energy of 2,910 keV from the $(p, 3p)$ reaction.

†The 2,600-keV transition observed in the $(p, 2p)$ reaction was not observed distinctly in the $(p, 3p)$ reaction, resulting in a likelihood maximum at 2,720(240) keV. The energy and the significance level of the transition at 2,910(43) keV were determined by fixing the neighbouring transition to 2,600 keV.

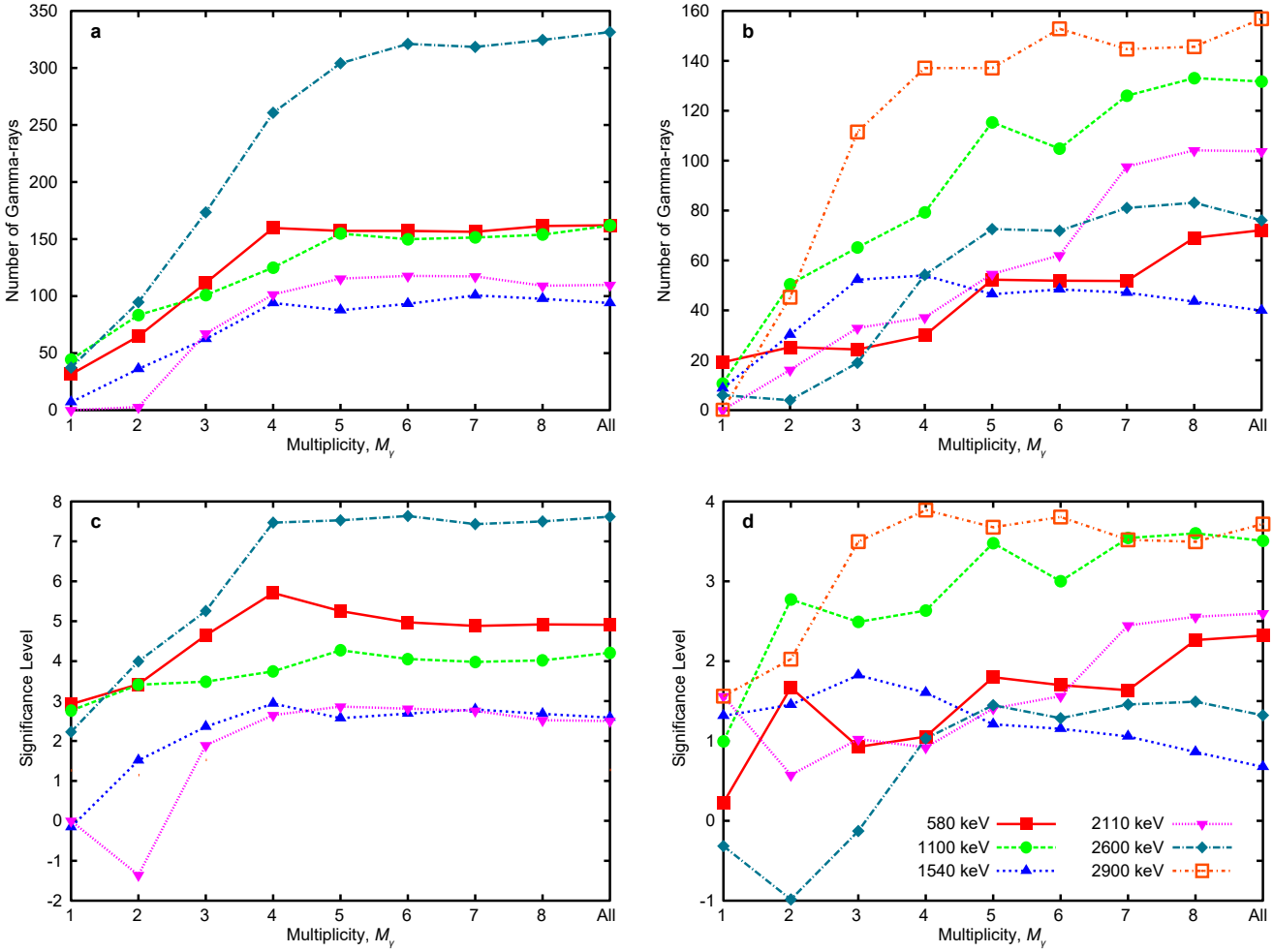

Extended Data Fig. 2 | Evolution of peak significance and fitted intensities as function of γ-ray multiplicity. **a,b**, Number of emitted γ rays obtained for fitted findividual transition **c,d**, Significance levels of individual transitions. The left side corresponds to the ^{79}Cu$(p, 2p)^{78}$Ni reaction and the right side to the ^{80}Zn$(p, 3p)^{78}$Ni reaction.